ACS APPLIED MATERIALS & INTERFACES

www.acsami.org

Research Article

Dual Porosity-Enhanced Antireflection Coatings with Continuous Gradient

Uiseok Hwang, Jae-Do Nam,* and Daeyeon Lee*

Cite This: *ACS Appl. Mater. Interfaces* 2023, 15, 40913−40922

Read Online

ACCESS | Metrics & More | Article Recommendations | Supporting Information

Downloaded via UNIV OF PENNSYLVANIA on November 17, 2023 at 20:24:38 (UTC).
See https://pubs.acs.org/sharingguidelines for options on how to legitimately share published articles.

ABSTRACT: The incorporation of porous structures into films and coatings can transform their properties for applications in optics, separation, electronics, and energy generation and storage. Packing nanoparticles (NPs) is a versatile approach for fabricating nanoporous films with a tunable structure and properties. The mechanical fragility of NP packing-based films and coatings, however, significantly impedes their widespread utilization. Although infiltrating a polymer into the interstices of these NP packings has been shown to enhance their mechanical durability, this method completely eliminates the porosity of the structures, compromising their properties and functionality. This study presents a new approach to fabricate highly loaded porous nanocomposite films with a gradient in the refractive index by infiltrating subsaturating amounts of poly(methyl methacrylate) (PMMA) into disordered packings of hollow silica NPs. We demonstrate that dual porosity is a critical feature that enhances their antireflection (AR) and mechanical properties. The hollow cores of NPs prevent a substantial increase in the refractive index of the resulting films. Moreover, the interparticle voids allow for mechanical reinforcement to occur when the NP packings are infiltrated with PMMA, making them even more suitable for AR coatings. The refractive index and gradient across the nanocomposites can be tailored by adjusting the amount of PMMA infiltrated into the NP packing, the shape of hollow NPs, and the annealing time. The nanocomposite coatings with a continuous gradient in refractive index exhibit excellent AR properties and enhanced mechanical durability. Combined with the unique structural tunability afforded by the dual porosity, this approach provides a scalable and effective way to create robust and graded nanoporous structures for various applications.

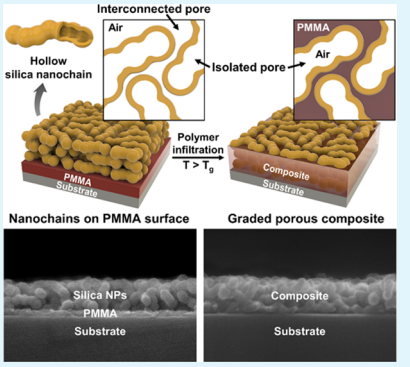

KEYWORDS: *nanoporous, capillary rise, hollow silica nanoparticles, nanocomposites, antireflection coatings, gradient*

INTRODUCTION

Nanoporous films with precisely engineered structures have been extensively explored in a wide range of fields, including optics, separations, electronics, and energy systems owing to their unique structures and properties.[1−9] For example, nanoporous films with refractive index < 1.3 are extremely useful as antireflection coatings (ARCs); such a low value of refractive index cannot be achieved with nonporous materials.[10−12] In the area of secondary batteries, nanoporous structures enable fast ion diffusion and increase the contact area between the electrode materials, thus improving the performance of the electrochemical system while also suppressing the growth of dendrites.[7,13−15]

Packing nanoparticles (NPs) is a versatile method to fabricate nanoporous films, which allows the use of various types of functional NPs yielding films with exceptional properties and functionality. Furthermore, the pore size and porosity can be easily controlled simply by adjusting the size and shape of NPs. Different types of NPs, for example, can be coated on transparent substrates to provide superhydrophilicity and antireflection (AR) properties as well as self-cleaning activity.[1,10] In the case of metal NPs, their films exhibit plasmonic colors depending on the spatial arrangement of the NPs, which can be controlled by the surface functional groups and shape of the NPs.[16,17] Although nanoporous films based on packing of NPs offer many benefits, they suffer from one critical shortcoming; these films are prone to abrasion and fracture even under a very small load, significantly restricting their widespread utilization. While previous studies have shown that the mechanical fragility of NP films can be mitigated through techniques like high-temperature sintering, atomic layer deposition, and hydrothermal treatment, controlling their structures remains challenging.[1,18,19] For instance, in the fabrication and utilization of ARCs for optical devices, graded porous structures are highly advantageous in suppressing reflection across a wide range of the visible light spectrum. However, most studies have generated gradients in films by sequentially coating multiple different materials onto substrates, which is complex and time-consuming.[10,20,21] Such

Received: May 20, 2023
Accepted: August 2, 2023
Published: August 16, 2023

ACS Publications

© 2023 American Chemical Society

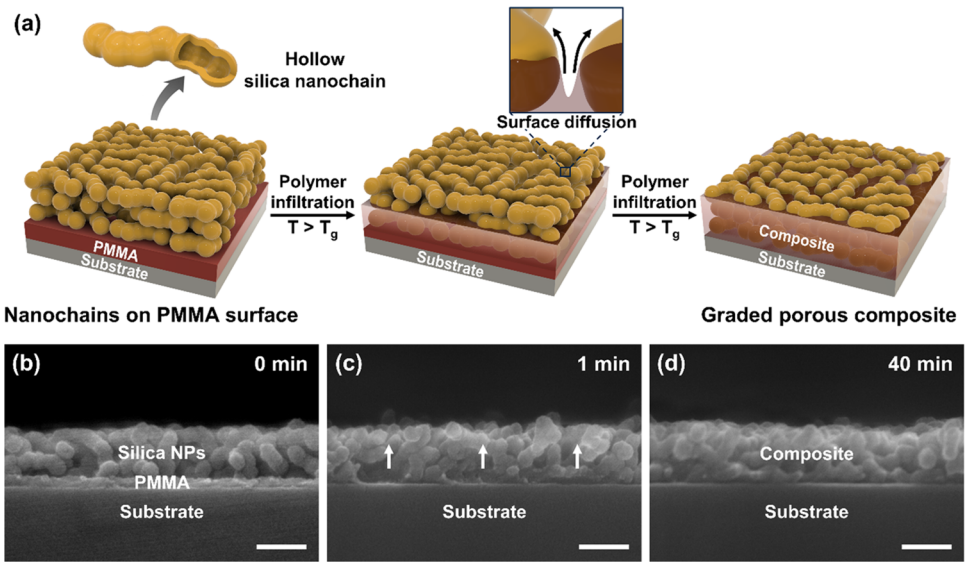

Figure 1. (a) Schematic illustration of the fabrication process of a highly loaded porous nanocomposite film with a continuous gradient incorporating hollow silica nanochains via UCaRI. Corresponding cross-sectional scanning electron microscopy (SEM) images of the bilayer film composed of a 130 nm silica NP layer on a 23 nm PMMA layer after (b–d) 40 min of heating at 150 °C. All scale bars are 100 nm.

multilayered coatings and films are not continuous due to the presence of interfaces between each layer, which could potentially degrade their performance.

Infiltrating polymers into a densely packed NP film via the capillary action of a molten polymer is a powerful way to drastically enhance its mechanical properties forming a nanocomposite film with extremely high NP loadings (>50 vol %).[22−25] In this method called capillary rise infiltration (CaRI), a bilayer film, consisting of a polymer layer and a layer of randomly packed NPs, is heated above the glass-transition temperature (T_g) of the polymer, which induces the polymer to infiltrate into the interstices between the NPs. However, mechanical reinforcement of films comes at the expense of compromising other important properties. The infiltration of polymer, in particular, increases the refractive index of the films, which would be detrimental to optical applications. A random packing of silica nanosphere possesses a refractive index of ∼1.3 or smaller, making them ideal for AR applications; however, complete infiltration of the interstitial pores by a polymer such as polystyrene (PS) increases the refractive index to ∼1.5, essentially eliminating AR properties from the film.[23] By infiltrating a subsaturating amount of polymer, this issue can be addressed while maintaining the refractive index of the film at a relatively low value. Furthermore, this approach is likely to enable the construction of porous structures with a continuous gradient.[24]

In this study, we show that both the AR and mechanical properties of ARCs can be enhanced by infiltrating a polymer into a disordered packing of hollow NPs. Two different types of pores present in these nanocomposite films, the hollow cores of NPs (isolated pores) and the interstitial pores of NP packings (interconnected pores), play distinct roles in enhancing the optical and mechanical properties of the porous nanocomposite films. The hollow structure of individual NPs leads to low-refractive-index coatings that have desirable AR properties, while the interparticle pores allow the infiltration of the polymer, which drastically enhances the mechanical durability of the ARCs. Moreover, the AR properties are further enhanced by creating a continuous gradient of the refractive index across the thickness of the coating. The porous nanocomposite coatings with a continuous gradient are fabricated by infiltrating subsaturating amounts of poly(methyl methacrylate) (PMMA) into disordered packings of hollow silica NPs of two different shapes: nanospheres and nanochains. We investigate the effect of particle shape and other processing parameters such as annealing time and the volume fraction of the polymer on the graded structure of these films. We also quantitatively distinguish and determine the porosities that originate from the isolated and interconnected pores. By taking advantage of the compositional gradient that develops during the undersaturated capillary rise infiltration (UCaRI) of polymers into the NP packings, graded ARCs with broadband AR properties in the visible spectrum are prepared. We demonstrate that these ARCs exhibit excellent mechanical robustness, maintaining their AR properties after multiple abrasion cycles.

RESULTS AND DISCUSSION

We fabricate porous nanocomposite films with a continuous gradient by preparing a bilayer of 23 nm thick PMMA and 130 nm thick disordered packing of hollow silica nanochains or nanospheres on silicon (Si) wafers and subsequently inducing infiltration of PMMA into the interstices of the NP films at 150 °C (>T_g of PMMA = ∼105 °C), as illustrated in Figure 1a; the volume of PMMA is not sufficient to fully fill the interstitial voids between the NPs. Our previous study has shown that, in such a case, the polymer first wicks into the interstices of the NP packing through capillary rise with a sharp front, and once the polymer under the NP layer is depleted, the infiltrated polymer undergoes surface diffusion creating a graded structure which ultimately evolves into a uniformly porous polymer-NP nanocomposite film as illustrated in Figure 1a.[24] At 150 °C, the fluidized PMMA starts to infiltrate into the NP layer, showing the PMMA-rich region at the bottom side of the film after 1 min of heating (Figure 1c). When the film is heated for 40 min, the PMMA diffused to the top surface of the NP layer, forming a porous nanocomposite film, as shown in Figure 1d.

https://doi.org/10.1021/acsami.3c07254
ACS Appl. Mater. Interfaces 2023, 15, 40913−40922

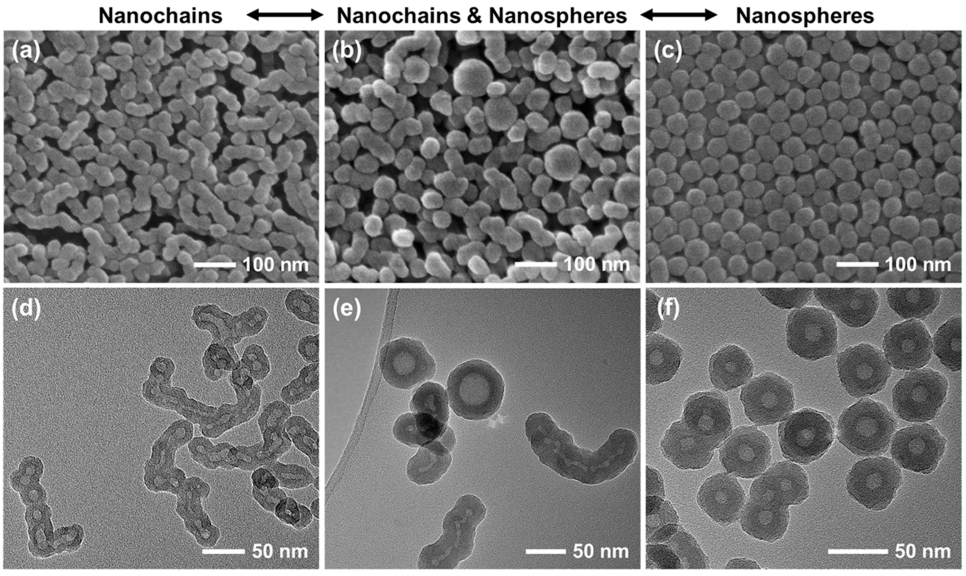

Figure 2. SEM images of hollow silica NPs with different shapes ranging from nanochain to nanosphere synthesized with different concentrations of TEOS of (a) 71.8, (b) 95.8, and (c) 119.7 mM. Corresponding transmission electron microscopy (TEM) images of the NPs with TEOS concentrations of (d) 71.8, (e) 95.8, and (f) 119.7 mM.

The shape of NPs is known to affect the structure, porosity, and mechanical properties of their disordered packings.[26] To test how the NP shape affects the structure and properties of ARCs, we synthesized hollow nanospheres and nanochains by modifying a previously reported method. This method relies on the condensation of a silica precursor, tetraethyl orthosilicate (TEOS), in the presence of a polyelectrolyte template, poly(acrylic acid) (PAA). It has been previously reported that the amounts of silica precursor and polyelectrolyte determine the shell thickness and diameter of spherical hollow silica NPs, respectively.[10,27] However, we find that varying the concentration of TEOS results in hollow silica NPs with different shapes, ranging from nanochains to nanospheres. Figure 2a–c shows the SEM images of hollow silica NPs synthesized with TEOS concentrations of 71.8, 95.8, and 119.7 mM. At a relatively low TEOS concentration of 71.8 mM, wormlike chains are generated (Figure 2a). The nanochains have an average diameter of 30 nm with a narrow distribution (CV < 6.7%), but their shape is irregular with the aspect ratio of ∼3.8; some nanochains have pendant particles linked to the backbone (∼28.2%). With an increased TEOS concentration of 95.8 mM, we obtain a mixture of nanochains and nanospheres with diameters of 38 and 74 nm, respectively (Figure 2b). The aspect ratio of the nanochains slightly decreases to ∼2.6 compared to those synthesized at the TEOS concentration of 71.8 mM. When the concentration of TEOS is further increased to 119.7 mM, fairly uniform nanospheres with an average diameter of 43 nm are produced (Figure 2c). When we increase the concentration of PAA from 0.013 to 0.028 mM with the concentration of TEOS kept constant at 119.7 mM, the diameter of the nanospheres is increased slightly from 43 ± 5 to 48 ± 7 nm (Figure S1).

As-synthesized hollow silica NPs are further characterized using TEM to investigate their structures. TEM images in Figure 2d–f clearly show that both nanochains and nanospheres have hollow cores stemming from the PAA aggregate template, which are removed during the rinsing step. The hollow nanochains have "peapod"-like structures with multiple spherical hollow cores; some of the cores are connected to form larger voids (Figure 2d,e). This structure suggests that these nanochains form through the partial coalescence of hollow nanospheres. Typically, hollow silica nanospheres are believed to form when TEOS is homogeneously hydrolyzed on spherical PAA aggregates in solution.[27,28] We believe, at low TEOS concentrations, a relatively small number of silica nuclei are generated that only partially cover PAA aggregates. The net surface charge of such a structure is likely low, inducing aggregation between these particles and, in turn, leading to the formation of various peapod-shaped nanochains.

N_2 adsorption–desorption isotherm of hollow silica nanochains further reveals the well-developed porous structure with their Brunauer–Emmett–Teller (BET) surface area of 354 m^2 g^{-1} and total pore volume of 0.449 cm^3 g^{-1} at P/P_0 = 0.977 (Figure S3a). As shown in Figure S3b, the pore size distribution curve clearly shows that the NPs have two different types of pores: the micropores (<2 nm) in the silica shells and the hollow cores of the NPs (∼30 nm).

Disordered packings of hollow silica NPs are prepared by spin-coating the NP suspensions on Si wafers. The nanochains and nanospheres synthesized at TEOS concentrations of 71.8 and 119.7 mM produce uniform films, whereas the mixture of the nanochains and nanospheres produced at the TEOS concentration of 95.8 mM results in the formation of nonuniform films, as shown in Figure S4. The refractive index of the film made of hollow silica nanochains is lower (n_{chain} = 1.15) than that of the film made of hollow nanospheres (n_{sphere} = 1.23), indicating that the anisotropy of the nanochains (aspect ratio = ∼3.8) induces sparser packing.[26,29] This result is interesting considering that a previous study showed that solid nanospheres and nanoellipsoids with aspect ratios of 1 and 4 generate disordered packings with an almost identical volume fraction of ∼0.65; the high degree of shape heterogeneity and the presence of pendant particles likely contribute to the lower packing density of these hollow nanochains.

The nanosphere film has an ideal refractive index value to function as an ARC on glass (n_{glass} = 1.52) and PMMA (n_{PMMA} = 1.49) substrates (Figure S5). Infiltration of a polymer such as

https://doi.org/10.1021/acsami.3c07254
ACS Appl. Mater. Interfaces 2023, 15, 40913–40922

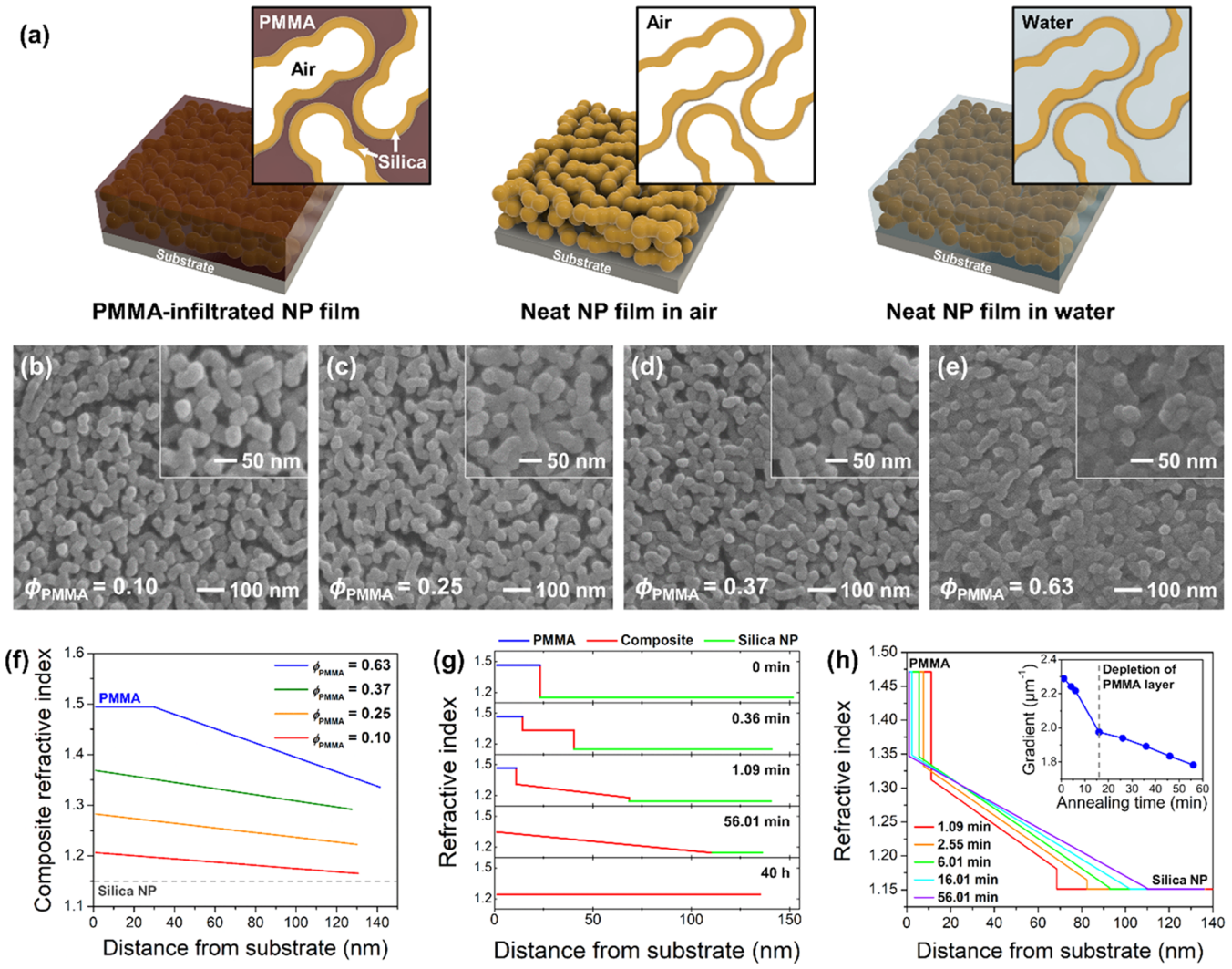

Figure 3. (a) Schematic illustrations of a PMMA-infiltrated hollow silica nanochain film and neat NP films in air and water with insets showing the morphology of the film filled with different materials (PMMA, air, and water). Top-down SEM images of bilayers composed of a 130 nm thick hollow silica nanochain layer atop a PMMA layer with different PMMA volume fractions (ϕ_{PMMA}) of (b) 0.10, (c) 0.25, (d) 0.37, and (e) 0.63 after 40 min at 150 °C. (f) Refractive index of the nanocomposites with different ϕ_{PMMA} values as a function of distance from substrate. (g, h) Refractive index of the bilayer film (ϕ_{PMMA} = 0.17) at various annealing intervals as a function of distance from substrate; the inset in (h) shows the corresponding refractive index gradient across the nanocomposite layer as a function of annealing time. The gradient of the nanocomposite layer at a given time is calculated by dividing the change in the refractive index within the nanocomposite layer by $h_{composite}$ (i.e., the absolute value of graph's slope of the nanocomposite layer in (h)).

PMMA into the interstices of NP packings, however, increases their refractive index; thus, the refractive index of PMMA-infiltrated hollow silica nanosphere film would be a bit too high to give optimal AR properties. In contrast, the hollow silica nanochain film makes an ideal coating for constructing nanocomposite ARCs due to its low refractive index. Furthermore, the randomly shaped nanochains with high anisotropy could mechanically interlock with each other when they are packed, enhancing their mechanical robustness and durability.[26]

The disordered packings of hollow silica NPs have structures that are distinct from those of their counterparts made with solid NPs. Hollow NP films possess two different types of voids: isolated pores from the hollow cores of NPs and interconnected pores from the interparticle voids. Disordered packings made with solid NPs, in contrast, only have interparticle voids. Our hypothesis is that the two different types of pores present in the disordered packings of hollow NPs would play distinctly important roles in enhancing the optical and mechanical properties of nanocomposite coatings for AR applications. Thus, it is critical to differentiate and quantify the porosity afforded by each pore type. To determine the volume fractions of two different types of pores as well as that of silica shell in the disordered packings of hollow NPs, we take advantage of the fact that PMMA does not infiltrate and fill the hollow cores of these NPs but fills the interparticle voids, as illustrated in Figure 3a. We first prepare PMMA-infiltrated hollow nanochain film of which the interstitial void is completely filled with PMMA. We find that when ϕ_{PMMA} = 0.37, no residual PMMA is left between the PMMA-infiltrated nanocomposite layer and the substrate upon the completion of CaRI (150 °C for 40 h). Any values of ϕ_{PMMA} greater than this critical value result in the presence of residual PMMA under the nanocomposite layer, indicating that the interparticle porosity of the NP film is 37%.[22] To determine the volume fractions of silica shell and void from hollow cores, the

https://doi.org/10.1021/acsami.3c07254
ACS Appl. Mater. Interfaces 2023, 15, 40913−40922

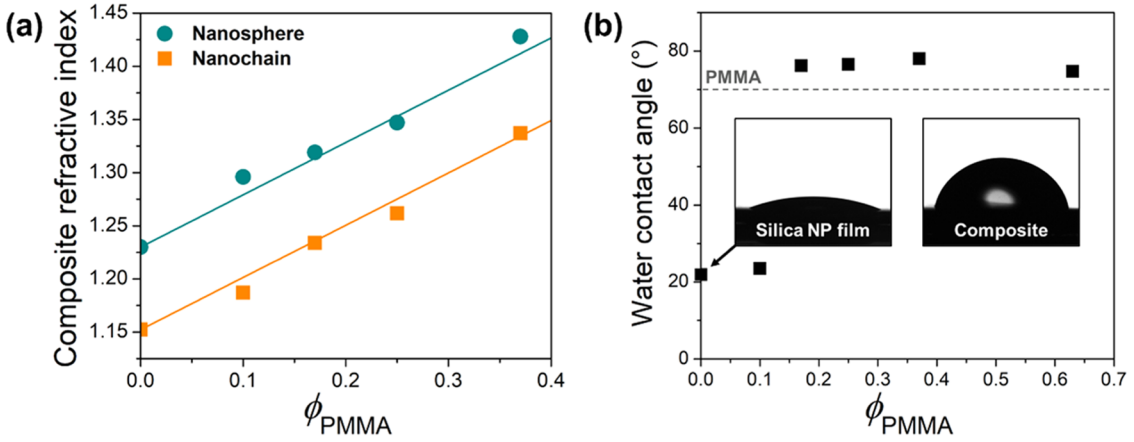

Figure 4. (a) Refractive index of nanocomposites incorporating nanochains and nanospheres annealed for 40 h as a function of ϕ_{PMMA}. The solid lines represent the estimated values based on ϕ_{PMMA}. (b) Water contact angles on the nanochain film and fully annealed nanochain nanocomposites as a function of ϕ_{PMMA}.

refractive index of the neat NP film is measured in air and in water, and a volume fraction-weighted mixing rule is applied (see Note S1 in the Supporting Information for the detailed calculation).[1,30,31] Water, unlike PMMA, readily fills both the interparticle voids and the hollow cores of the NPs (Figure 3a). Based on these measurements and calculations, the void volume fraction of hollow cores of nanochains in the entire film is 29.3%, and thus the overall porosity of the NP film is 66.5%. The refractive index of the silica shell of nanochain, determined using the method described in the Supporting Information, is 1.46, in excellent agreement with the reported refractive index value of amorphous silica.[32−35]

Prior studies have shown that incorporating a refractive index gradient across the thickness of a film is an efficient method to produce a broadband ARC.[21,36,37] To produce such a structure, we infiltrate subsaturating amounts of PMMA into the disordered packings of hollow NPs. To control the extent of UCaRI, we define the volume fraction of PMMA in each film as $\phi_{PMMA} = \frac{h_{PMMA}}{h_{NP}}$, where h_{PMMA} and h_{NP} are the thicknesses of the PMMA layer and hollow silica NP layer, respectively. PMMA layers with thicknesses of 13, 33, 48, and 82 nm (h_{PMMA}) are prepared by adjusting the spin coating speed, while the thickness of silica NP layer (h_{NP}) is kept constant at 130 nm. Upon UCaRI, the film with the lowest ϕ_{PMMA} of 0.10 displays clear outlines of the NPs and the interparticle voids (Figure 3b), whereas the voids cannot be discerned with the film that was prepared with ϕ_{PMMA} = 0.63 (Figure 3e).

At ϕ_{PMMA} = 0.37, 40 min of annealing time is not sufficient to produce a nanocomposite film with a homogeneous structure through its thickness, as confirmed by the SEM image of the top surface of the film, showing several interparticle voids (Figure 3d). To describe the structure of these films accurately, we determine the refractive index of the films through the thickness after 40 min of heating at 150 °C using the ellipsometer, as shown in Figure 3f; we consider a simple linear gradient of the refractive index in the polymer-infiltrated nanocomposite layer. The graded Cauchy model assumes 10 layers within the Cauchy domain and provides the gradient in the refractive index within this domain.[38−40] All four nanocomposite films with different ϕ_{PMMA}'s exhibit gradients in the refractive index across the film thickness; the refractive index of films decreases toward the top surface of the films (Figure 3f). This implies that the PMMA gradually spreads within the silica NP layer upon annealing, forming high loaded (volume fraction of NPs >50%) nanocomposites with a continuously graded refractive index. The refractive index values at the top surface of the films are higher than that of native hollow silica nanochain film (n_{chain} = 1.15), indicating that small amounts of polymer have reached the top surfaces of these films between the nanochains, consistent with the top-down SEM images of the films, as seen in Figure 3b−e. With increasing ϕ_{PMMA}, the overall refractive index of the film increases as the higher fraction of the interparticle voids is filled with PMMA (n_{PMMA} = 1.49).

Interestingly, the bilayer with ϕ_{PMMA} = 0.63, which has an oversaturating amount of PMMA, evolves into a graded structure even though there is a residual PMMA layer under the nanocomposite layer. Such a structure is different from the one that has been typically observed when an oversaturating amount of polystyrene (PS) is infiltrated into a disordered packing of silica NPs.[41] In these cases, a gradient is not formed throughout the entire infiltration process. During polymer infiltration, a sharp front divides the infiltrated nanocomposite layer and the uninfiltrated NP layer until the completion of CaRI.

To understand the difference in the infiltration behavior of PMMA and PS into silica NP packings, the structural evolution of the films at various annealing stages is monitored by following the change in the refractive index of PMMA, PMMA-infiltrated nanocomposite, and uninfiltrated NP layers, as shown in Figure 3g,h. Before annealing, the bilayer consists of an NP layer (n_{chain} = 1.15) atop a PMMA layer (n_{PMMA} = 1.49) (Figure 3g). Upon annealing, an almost fully filled nanocomposite layer (the PMMA fraction in the nanocomposite layer, f_{PMMA} = 0.34) is instantly formed between the PMMA and NP layers at 0.36 min. At 1.09 min, the nanocomposite layer exhibits graded refractive index across the entire NP layer decreasing toward the top surface of film, even before the PMMA layer is completely depleted; this result again is distinct from our previous result which showed that PS, which is known to have relatively weak interactions with silica, starts surface diffusion on the surface of silica NPs once the residual PS between the nanocomposite layer and the substrate is completely consumed.[24] The ability of PMMA to diffuse on the surface of NPs even before the complete consumption of

https://doi.org/10.1021/acsami.3c07254
ACS Appl. Mater. Interfaces 2023, 15, 40913−40922

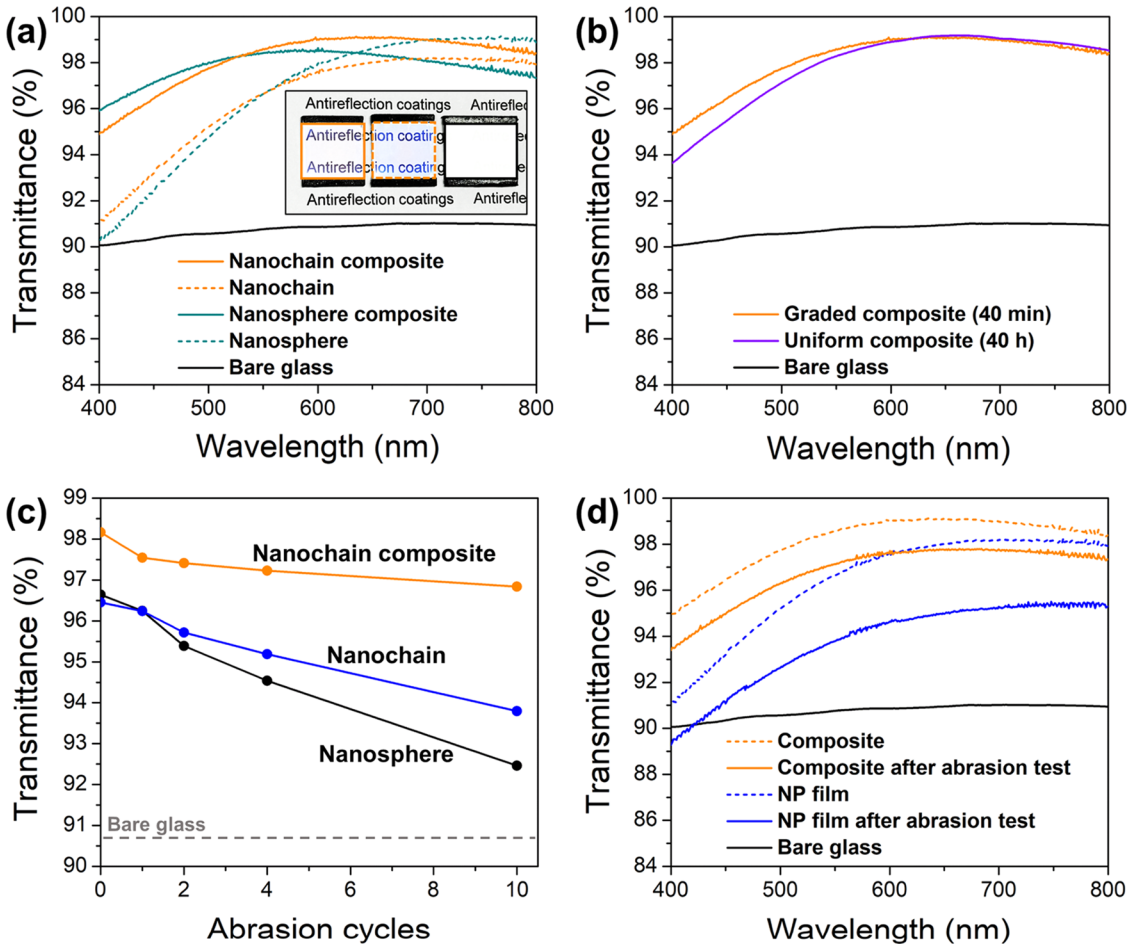

Figure 5. (a) Transmittance spectra of different ARCs on glass substrates with the inset showing a digital photograph of light reflections from nanochain nanocomposite, neat nanochain film, and bare glass (from left to right). Both sides of glass substrates are coated with ARCs. (b) Transmittance spectra of nanochain nanocomposite ARCs with different annealing times producing graded and uniform structures. (c) Average visible light transmittance of different ARCs on glass substrates as a function of abrasion cycle, comparing their mechanical durability, and (d) the corresponding transmittance spectra of the ARCs after 10 abrasion cycles.

the PMMA layer is likely due to its high affinity toward the silica surface. PMMA has strong interactions with silica due to hydrogen bonding between the silanol group of silica and the ester carbonyl group of methacrylate group.[42] The ellipsometry result in this intermediate stage is supported by the cross-sectional SEM image of the film (Figure 1c). Subsequently, the gradient in the nanocomposite layer and the thickness of the residual PMMA layer decrease gradually until 56.01 min, as shown in Figure 3h. Finally, after 40 h, a macroscopically uniform porous nanocomposite is formed ($n_{composite}$ = 1.23). We find that the infiltration rate of PMMA changes when the PMMA layer is depleted (~16 min), as indicated by different slopes at the 16 min mark, as shown in the inset of Figure 3h. Based on this result, it would take 6.6 h to reach uniform composition across the nanocomposite layer (i.e., 0 μm^{-1}).

By annealing the nanocomposites with nanochains or nanospheres with $\phi_{PMMA} \leq 0.37$ for 40 h, at which polymer distributes uniformly throughout the NP packings (i.e., gradient across the nanocomposite = ~0 μm^{-1}), we obtain macroscopically uniform porous nanocomposite films with the refractive index ranging 1.19−1.34 and 1.30−1.43, respectively (Figure 4a). The refractive index of the uniform nanocomposites increases linearly with ϕ_{PMMA}, and the values match well with the estimated refractive indices of the nanocomposite films based on the relative thicknesses of the NP and PMMA layers and the interparticle porosity (see Note S1 in the Supporting Information).

We also confirm the presence of polymer near the top surface of the nanocomposite films by measuring the water contact angles (Figure 4b). The water contact angle on the neat NP film is 16°. The contact angle on a bilayer consisting of a 130 nm NP layer atop a 23 nm PMMA layer before annealing is 22°, closely matching that on the neat NP film. The fully annealed nanocomposites (i.e., annealed for 40 h) with $\phi_{PMMA} > 0.10$ exhibit contact angles larger than 74°, indicating the presence of polymer at or near the top surface of the films. This value is slightly greater than the contact angle of water on the neat PMMA film (70°), possibly due to the roughness of the nanocomposite films. For the nanocomposite with $\phi_{PMMA} = 0.10$, the contact angle is 24°, indicating that the surface of such a nanocomposite is predominantly silica NPs.

The refractive index and thickness of the coating are the main factors that determine the magnitude of destructive interference by reflected lights in ARCs. We can control these variables independently by adjusting the amount of PMMA infiltrated into the NP layer (i.e., ϕ_{PMMA}) and the thickness of the NP layer which depends on the spin coating speed, respectively. Taking these factors into account, we produce

https://doi.org/10.1021/acsami.3c07254
ACS Appl. Mater. Interfaces 2023, 15, 40913−40922

nanocomposite ARCs with ϕ_{PMMA} = 0.17 on both sides of a glass slide using hollow NPs with a thickness of 130 nm (see Figure S6 in the Supporting Information for a detailed analysis of the structural evolution of these nanocomposite films with ϕ_{PMMA} = 0.17). Figure 5a shows the transmittance of nanocomposite ARCs incorporating nanochains or nanospheres with an annealing time of 40 min along with the spectra for glass slides coated with respective NP coatings without PMMA; these nanocomposite ARCs have graded structures across the layer, as confirmed by ellipsometry analysis (Figures 3f and S7). When coated with nanochain and nanosphere films with refractive indices of 1.15 and 1.23, the respective films provide average transmittance of 96.5 and 96.6% with maxima of 98.3 and 99.2% at 759 and 767 nm. In contrast, glass substrates coated with the graded nanocomposite ARCs incorporating nanochains or nanospheres exhibit remarkedly broader AR properties than those coated with the NP films with enhanced transmittance of 97.9 and 98.2% with the maxima of 98.6 and 99.1% at 600 and 635 nm, respectively. With the same ϕ_{PMMA} of 0.17, the nanochain nanocomposite coating outperforms the nanosphere nanocomposite coating due to its lower refractive index (1.23 for nanochains vs 1.32 for nanospheres). The inset photo in Figure 5a reveals the visual impact of the ARCs, showing that these coatings effectively suppress the light reflection from glass substrates. In particular, the ARC based on polymer-infiltrated nanochains exhibits the strongest suppression of light reflection on glass.

To elucidate the effect of graded structure on the AR performance, we compare the transmittance of the nanochain nanocomposite ARCs (ϕ_{PMMA} = 0.17) annealed for 40 min and 40 h (Figure 5b). Once the nanocomposite ARCs are fully annealed for 40 h, transmittance in the low-wavelength region of 400−600 nm is decreased due to the loss of the graded structure and thus provides a narrower band with the reduced average transmittance of 97.9%.

In addition to the excellent optical transmittance, the robust mechanical durability of ARCs is another important factor that must be considered for their practical use. We carry out an abrasion test for different coatings by applying a normal pressure of ∼1.2 kPa (which is equivalent to the pressure generated by stacking 9 smartphones on the surface) on top of a low lint wiper that is placed on the ARC and sliding the wiper across the surface multiple times. After 10 abrasion cycles, neat NP coatings of nanochain and nanosphere almost completely lose their AR properties, exhibiting average transmittance of 93.8 and 92.5%, respectively, as shown in Figure 5c,d; the nanochain coating shows less decrease (2.7%) in transmittance than the nanosphere coating (4.1%), possibly due to the mechanical interlocking between the NPs.[26] The graded nanocomposite ARC incorporating nanochains and PMMA (ϕ_{PMMA} = 0.17) with an annealing time of 40 min shows only a minor decrease of 1.3% in the transmittance to 96.8%. Such exceptional mechanical robustness of the nanocomposite ARC originates from the fact that the PMMA chains between the interlocked nanochains provide bridging, enhancing their mechanical durability.[25] The NP coating experiences significant deterioration when a stronger normal pressure of 10 kPa is applied, exposing the bare glass due to the complete removal of the NPs (Figure S8). In contrast, the transmittance of the nanocomposite ARC at 600 nm stays above that of bare glass even after six cycles of abrasion, demonstrating the mechanical robustness of these ARCs.

We also compare the optical behaviors of the ARCs across the UV range (Figure S9). The glass substrate absorbs strongly in the UV range; thus, the transmittance is very low below 350 nm. In the wavelength range 350−400 nm, the nanochain nanocomposite ARCs enhance the light transmittance, while the neat nanochain film exhibits a decrease in performance compared with bare glass, likely due to scattering. The graded nanocomposite gives a higher increase in transmittance (3.5%) from the bare glass than the uniform nanocomposite ARC (2.4%), indicating that the graded structure can provide broad-spectrum AR properties, including those in the UV range.

Thermal stability is another critical factor in the practical applications of ARCs. When heated above the T_g of the polymer, graded nanocomposite ARCs undergo a transition into uniformly structured nanocomposites. Thus, the graded nanocomposite can maintain its structural integrity up to T_g of PMMA. In contrast, uniform nanocomposite films would remain stable until the degradation temperature of PMMA (above ∼240 °C) is reached;[43] it is interesting to note that our recent study has shown that extreme nanoconfinement can substantially enhance the thermal stability of polymers in these CaRI films.[44,45] The rheology of the polymers (i.e., the effective viscosity) can also be affected by the confinement. For unentangled polymers, e.g., confinement can drastically increase the effective viscosity of the polymer compared to the same polymer in bulk. In contrast, confinement can also induce a substantial decrease in the effective viscosity for highly entangled polymers due to the disentanglement effect.[41,44−46]

While this work focuses on the fabrication of ARCs on rigid glass substrates, our ongoing work focuses on producing ARCs on flexible substrates and examining how these ARCs respond to different modes of mechanical loads such as bending.

CONCLUSIONS

We have studied the fundamental processing structure−property relationship of porous nanocomposite films with a continuous gradient fabricated via UCaRI of PMMA into disordered packings of hollow silica nanochains and nanospheres and showed that these nanocomposite coatings have excellent broadband AR properties on glass substrates. More importantly, we show that two different types of pores present in the disordered packings of hollow NPs play distinct roles in enhancing the performance of these ARCs. While the hollow cores of NPs maintain the refractive index of the nanocomposite film at a low value, making them ideal for AP applications, the interstitial pores enable the infiltrated PMMA to enhance the mechanical durability of the resulting film. We demonstrate that a continuous gradient in the refractive index across the film thickness imbues these ARCs with broadband AR properties over the visible light spectrum. The refractive index and gradient of the nanocomposite coatings can be precisely controlled independently by adjusting the infiltration amount of PMMA and annealing time to give optimized conditions for excellent AR properties. Our strategy of using hollow silica NPs and creating a graded structure via UCaRI presents a potentially scalable technique for the construction of graded nanoporous structures in highly loaded nanocomposites with various combinations of polymers and NPs, making them extremely useful and attractive for a wide range of applications.

https://doi.org/10.1021/acsami.3c07254
ACS Appl. Mater. Interfaces 2023, 15, 40913−40922

EXPERIMENTAL SECTION

Materials. Tetraethyl orthosilicate (TEOS, 99%) and ammonium hydroxide solution (28 wt %) are purchased from Sigma-Aldrich. An aqueous solution of poly(acrylic acid) (PAA) (50 wt %, M_w = ∼5000 g mol^{-1}) is purchased from Polyscience, Inc. PMMA (M_w = 49,500 g mol^{-1}, PDI = 1.1) is purchased from Polymer Source, Inc. (Canada).

Synthesis of Hollow Silica NPs. Hollow silica NPs with different shapes are synthesized by a modified Stöber method.[27,47] First, PAA (0.35 g) dissolved in an ammonium hydroxide solution (17.5 mL) is mixed with ethanol (450 mL), followed by the injection of five aliquots of TEOS totaling 7.5, 10, and 12.5 mL, corresponding to the TEOS concentrations of 71.8, 95.8, and 119.7 mM, respectively, at 1 h time intervals under vigorous magnetic stirring at room temperature. After 10 h, light blue colloids containing silica NPs filled with PAA templates are obtained. The resulting colloids are centrifuged several times with deionized water and ethanol and then redispersed in ethanol.

Fabrication of Polymer-Infiltrated Hollow Silica NP Films. Prior to film deposition, silicon wafers are cut into approximately 1.5 × 1.5 cm^2 squares, rinsed with isopropyl alcohol and deionized water, and subsequently dried with nitrogen. The wafers are oxygen plasma-treated for 5 min for further cleaning. The PMMA solution (1−2 wt %) is prepared by dissolving PMMA in toluene. The hollow silica NP dispersions (4−8 wt %) are sonicated for 2 h, followed by filtering using syringe filters with a cutoff of 450 nm. To generate nanocomposite films, the PMMA layer is first deposited onto the substrates via spin coating (WS-400BZ-6NPP/Lite spin coater, Laurell Technologies Corporation). Then, the PMMA film is oxygen plasma-treated for 5 s to render the film surface hydrophilic, on which the hollow silica NP layer is spin-coated to form a bilayer film. The thickness of each layer is controlled by changing the rotation speed (2000−10,000 rpm). The prepared bilayers are thermally annealed in an oven at 150 °C.

Fabrication of ARCs. ARCs are prepared on glass substrates by using the aforementioned method. Glass slides are cut into approximately 3 × 3 cm^2 squares and oxygen plasma-treated for 5 min. PMMA layer and hollow silica NP layer are sequentially spin-coated on both sides of the glass substrates, followed by thermal annealing in an oven at 150 °C to yield nanocomposite ARCs.

Characterization. PMMA infiltration into the interparticle voids of the hollow silica NP layer is monitored using spectroscopic ellipsometry (α-SE, J.A. Woollam Co., Inc.) while the samples are annealed using a heating stage (Linkam THMS 350 V, U.K.) with a temperature resolution of 0.1 °C. The ellipsometry data are collected between λ = 380 and 900 nm at an incident angle of 70° and analyzed using the CompleteEASE software. The raw ellipsometry data, $\Psi(\lambda)$ and $\Delta(\lambda)$, are fit using the Cauchy model ($n(\lambda) = A + B/\lambda^2$, $k(\lambda) = 0$), where A and B are optical constants, and n and k are the real and imaginary parts of the refractive index, respectively.[22,23] All Cauchy modeling is performed with low mean square errors (<15). The thickness and refractive index of the deposited films before and after annealing are also determined using the ellipsometer.

The size and structure of the samples are examined using a field emission scanning electron microscope (FE-SEM) (JSM-7500F, JEOL, Japan) and a high-resolution transmission electron microscope (HRTEM) (JEM-F200, JEOL, Japan). The statistical analysis is performed by measuring the size and thickness of a minimum of 50 nanoparticles in SEM and TEM images using ImageJ software. The transmittance of the samples is characterized in the range of λ = 400−800 nm using a UV−vis spectrophotometer (Cary 5000, Varian). The contact angles of water on the film surfaces are determined using a goniometer (Biolin Scientific, Attention, Sweden). The specific surface area and pore size distribution are measured by nitrogen adsorption−desorption isotherms (ASAP2020, Micromeritics) and calculated by the Brunauer−Emmett−Teller (BET) method.

ASSOCIATED CONTENT

Supporting Information

The Supporting Information is available free of charge at https://pubs.acs.org/doi/10.1021/acsami.3c07254.

SEM images of hollow silica spheres synthesized with different PAA concentrations; correlation of synthetic conditions and structures of hollow silica NPs; statistical analysis of hollow silica nanochains; BET measurement data of hollow silica nanochains; refractive index calculation; in situ spectroscopic ellipsometry data; refractive index of nanosphere nanocomposites; abrasion test results with a normal pressure of 10 kPa; and transmittance spectra of ARCs across the UV−vis range (PDF)

AUTHOR INFORMATION

Corresponding Authors

Jae-Do Nam − *Department of Polymer Science and Engineering, Sungkyunkwan University, Suwon 16419, Republic of Korea;* orcid.org/0000-0001-7682-7926; Email: jdnam@skku.edu

Daeyeon Lee − *Department of Chemical and Biomolecular Engineering, School of Engineering and Applied Science, University of Pennsylvania, Philadelphia, Pennsylvania 19104, United States;* orcid.org/0000-0001-6679-290X; Email: daeyeon@seas.upenn.edu

Author

Uiseok Hwang − *Department of Chemical and Biomolecular Engineering, School of Engineering and Applied Science, University of Pennsylvania, Philadelphia, Pennsylvania 19104, United States; Department of Polymer Science and Engineering, Sungkyunkwan University, Suwon 16419, Republic of Korea*

Complete contact information is available at: https://pubs.acs.org/10.1021/acsami.3c07254

Author Contributions

All authors discussed the results, critically revised the manuscript, and gave the final approval.

Notes

The authors declare no competing financial interest.

ACKNOWLEDGMENTS

This work was supported by Penn MRSEC through NSF (NSF DMR 1720530) and NSF CBET-1933704. The authors thank Dr. Baekmin Kim, Dr. Jae-Hyun Kim, and Dr. Joseph Rosenfeld for helpful discussions and technical support. U.H. acknowledges the support from the Korea Institute for Advancement of Technology (KIAT) grant funded by the Korea Government (MOTIE) (P0017305, Human Resource Development Program for Industrial Innovation (Global)).

REFERENCES

(1) Lee, D.; Rubner, M. F.; Cohen, R. E. All-Nanoparticle Thin-Film Coatings. *Nano Lett.* **2006**, *6*, 2305−2312.

(2) Walheim, S.; Schäffer, E.; Mlynek, J.; Steiner, U. Nanophase-Separated Polymer Films as High-Performance Antireflection Coatings. *Science* **1999**, *283*, 520−522.

(3) Hiller, J. A.; Mendelsohn, J. D.; Rubner, M. F. Reversibly Erasable Nanoporous Anti-Reflection Coatings from Polyelectrolyte Multilayers. *Nat. Mater.* **2002**, *1*, 59−63.

(4) Dürr, M.; Schmid, A.; Obermaier, M.; Rosselli, S.; Yasuda, A.; Nelles, G. Low-Temperature Fabrication of Dye-Sensitized Solar Cells by Transfer of Composite Porous Layers. *Nat. Mater.* **2005**, *4* (8), 607−611.
(5) Lee, J.; Jang, J. H.; Chae, H.-R.; Lee, S. H.; Lee, C.-H.; Park, P.-K.; Won, Y.-J.; Kim, I.-C. A Facile Route to Enhance the Water Flux of a Thin-Film Composite Reverse Osmosis Membrane: Incorporating Thickness-Controlled Graphene Oxide into a Highly Porous Support Layer. *J. Mater. Chem. A* **2015**, *3* (44), 22053−22060.
(6) Klaysom, C.; Marschall, R.; Moon, S.-H.; Ladewig, B. P.; Lu, G. Q. M.; Wang, L. Preparation of Porous Composite Ion-Exchange Membranes for Desalination Application. *J. Mater. Chem.* **2011**, *21* (20), 7401−7409.
(7) Yang, Z.; Qiu, L.; Zhang, M.; Zhong, Y.; Zhong, B.; Song, Y.; Wang, G.; Liu, Y.; Wu, Z.; Guo, X. Carbon Dioxide Solid-Phase Embedding Reaction of Silicon-Carbon Nanoporous Composites for Lithium-Ion Batteries. *Chem. Eng. J.* **2021**, *423*, No. 130127.
(8) Kim, S.; Hwang, U.; Yang, K.; Cho, M.; Nam, J.-D.; Lee, Y. Constructing Robust Zincophilic−Channels on Zn Anode for Long-Life Zn-Ion Batteries. *Chem. Eng. J.* **2022**, *440*, No. 135822.
(9) Hudiono, Y.; Choi, S.; Shu, S.; Koros, W. J.; Tsapatsis, M.; Nair, S. Porous Layered Oxide/Nafion Nanocomposite Membranes for Direct Methanol Fuel Cell Applications. *Microporous Mesoporous Mater.* **2009**, *118*, 427−434.
(10) Du, Y.; Luna, L. E.; Tan, W. S.; Rubner, M. F.; Cohen, R. E. Hollow Silica Nanoparticles in UV−Visible Antireflection Coatings for Poly(methyl methacrylate) Substrates. *ACS Nano* **2010**, *4*, 4308−4316.
(11) Zhang, X.; Lan, P.; Lu, Y.; Li, J.; Xu, H.; Zhang, J.; Lee, Y.; Rhee, J. Y.; Choy, K.-L.; Song, W. Multifunctional Antireflection Coatings Based on Novel Hollow Silica−Silica Nanocomposites. *ACS Appl. Mater. Interfaces* **2014**, *6*, 1415−1423.
(12) Reid, B.; Taylor, A.; Chen, Y.; Schmidt-Hansberg, B.; Guldin, S. Robust Operation of Mesoporous Antireflective Coatings under Variable Ambient Conditions. *ACS Appl. Mater. Interfaces* **2018**, *10*, 10315−10321.
(13) Xue, P.; Guo, C.; Li, L.; Li, H.; Luo, D.; Tan, L.; Chen, Z. A MOF-Derivative Decorated Hierarchical Porous Host Enabling Ultrahigh Rates and Superior Long-Term Cycling of Dendrite-Free Zn Metal Anodes. *Adv. Mater.* **2022**, *34*, No. 2110047.
(14) Zhang, X.; Hui, Z.; King, S. T.; Wu, J.; Ju, Z.; Takeuchi, K. J.; Marschilok, A. C.; West, A. C.; Takeuchi, E. S.; Wang, L.; Yu, G. Gradient Architecture Design in Scalable Porous Battery Electrodes. *Nano Lett.* **2022**, *22*, 2521−2528.
(15) Chen, L.; Zhang, J.; Tong, R.-A.; Zhang, J.; Wang, H.; Shao, G.; Wang, C.-A. Excellent Li/Garnet Interface Wettability Achieved by Porous Hard Carbon Layer for Solid State Li Metal Battery. *Small* **2022**, *18*, No. 2106142.
(16) Liu, L.; Aleisa, R.; Zhang, Y.; Feng, J.; Zheng, Y.; Yin, Y.; Wang, W. Dynamic Color-Switching of Plasmonic Nanoparticle Films. *Angew. Chem., Int. Ed.* **2019**, *58*, 16307−16313.
(17) Lee, S.; Sim, K.; Moon, S. Y.; Choi, J.; Jeon, Y.; Nam, J.-M.; Park, S.-J. Controlled Assembly of Plasmonic Nanoparticles: From Static to Dynamic Nanostructures. *Adv. Mater.* **2021**, *33*, No. 2007668.
(18) Dafinone, M. I.; Feng, G.; Brugarolas, T.; Tettey, K. E.; Lee, D. Mechanical Reinforcement of Nanoparticle Thin Films Using Atomic Layer Deposition. *ACS Nano* **2011**, *5*, 5078−5087.
(19) Gemici, Z.; Shimomura, H.; Cohen, R. E.; Rubner, M. F. Hydrothermal Treatment of Nanoparticle Thin Films for Enhanced Mechanical Durability. *Langmuir* **2008**, *24*, 2168−2177.
(20) Chhajed, S.; Schubert, M. F.; Kim, J. K.; Schubert, E. F. Nanostructured Multilayer Graded-Index Antireflection Coating for Si Solar Cells with Broadband and Omnidirectional Characteristics. *Appl. Phys. Lett.* **2008**, *93*, No. 251108.
(21) Ji, C.; Zhang, Z.; Omotosho, K. D.; Berman, D.; Lee, B.; Divan, R.; Guha, S.; Shevchenko, E. V. Porous but Mechanically Robust All-Inorganic Antireflective Coatings Synthesized using Polymers of Intrinsic Microporosity. *ACS Nano* **2022**, *16*, 14754−14764.
(22) Huang, Y.-R.; Jiang, Y.; Hor, J. L.; Gupta, R.; Zhang, L.; Stebe, K. J.; Feng, G.; Turner, K. T.; Lee, D. Polymer Nanocomposite Films with Extremely High Nanoparticle Loadings via Capillary Rise Infiltration (CaRI). *Nanoscale* **2015**, *7*, 798−805.
(23) Kim, B. Q.; Qiang, Y.; Turner, K. T.; Choi, S. Q.; Lee, D. Heterostructured Polymer-Infiltrated Nanoparticle Films with Cavities via Capillary Rise Infiltration. *Adv. Mater. Interfaces* **2021**, *8* (3), No. 2001421.
(24) Hor, J. L.; Jiang, Y.; Ring, D. J.; Riggleman, R. A.; Turner, K. T.; Lee, D. Nanoporous Polymer-Infiltrated Nanoparticle Films with Uniform or Graded Porosity via Undersaturated Capillary Rise Infiltration. *ACS Nano* **2017**, *11* (3), 3229−3236.
(25) Qiang, Y.; Pande, S. S.; Lee, D.; Turner, K. T. The Interplay of Polymer Bridging and Entanglement in Toughening Polymer-Infiltrated Nanoparticle Films. *ACS Nano* **2022**, *16*, 6372−6381.
(26) Zhang, L.; Feng, G.; Zeravcic, Z.; Brugarolas, T.; Liu, A. J.; Lee, D. Using Shape Anisotropy to Toughen Disordered Nanoparticle Assemblies. *ACS Nano* **2013**, *7*, 8043−8050.
(27) Wan, Y.; Yu, S.-H. Polyelectrolyte Controlled Large-Scale Synthesis of Hollow Silica Spheres with Tunable Sizes and Wall Thicknesses. *J. Phys. Chem. C* **2008**, *112*, 3641−3647.
(28) Hwang, U.; Kim, J.; Kim, N.-Y.; Choi, K.; Chung, J.-Y.; Kim, T.; Suhr, J.; Nam, J.-D. Surface Charge Control of Hierarchical Ceria/Silica Hybrid Shells for Enhanced Dispersion Stability. *Appl. Surf. Sci.* **2022**, *571*, No. 151173.
(29) Buskens, P.; Burghoorn, M.; Mourad, M. C. D.; Vroon, Z. Antireflective Coatings for Glass and Transparent Polymers. *Langmuir* **2016**, *32*, 6781−6793.
(30) Braun, M. M.; Pilon, L. Effective Optical Properties of Non-Absorbing Nanoporous Thin Films. *Thin Solid Films* **2006**, *496*, 505−514.
(31) Zimmermann, L.; Weibel, M.; Caseri, W.; Suter, U. W.; Walther, P. Polymer Nanocomposites with "Ultralow" Refractive Index. *Polym. Adv. Technol.* **1993**, *4*, 1−7.
(32) Lee, D.; Omolade, D.; Cohen, R. E.; Rubner, M. F. pH-Dependent Structure and Properties of TiO_2/SiO_2 Nanoparticle Multilayer Thin Films. *Chem. Mater.* **2007**, *19*, 1427−1433.
(33) Lee, D.; Gemici, Z.; Rubner, M. F.; Cohen, R. E. Multilayers of Oppositely Charged SiO_2 Nanoparticles: Effect of Surface Charge on Multilayer Assembly. *Langmuir* **2007**, *23*, 8833−8837.
(34) Huang, Y.-F.; Chattopadhyay, S.; Jen, Y.-J.; Peng, C.-Y.; Liu, T.-A.; Hsu, Y.-K.; Pan, C.-L.; Lo, H.-C.; Hsu, C.-H.; Chang, Y.-H.; et al. Improved Broadband and Quasi-Omnidirectional Anti-Reflection Properties with Biomimetic Silicon Nanostructures. *Nat. Nanotechnol.* **2007**, *2*, 770−774.
(35) Lim, Y.; Lee, S.-H.; Li, Y.; Kim, S.-H.; Kang, T. H.; Suh, Y. D.; Lee, S.; Kim, Y.; Yi, G.-R. Transparent and UV-Reflective Photonic Films and Supraballs Composed of Hollow Silica Nanospheres. *Part. Part. Syst. Charact.* **2020**, *37*, No. 1900405.
(36) Ruud, C. J.; Cleri, A.; Maria, J.-P.; Giebink, N. C. Ultralow Index SiO_2 Antireflection Coatings Produced via Magnetron Sputtering. *Nano Lett.* **2022**, *22*, 7358−7362.
(37) Cai, J.; Qi, L. Recent Advances in Antireflective Surfaces based on Nanostructure Arrays. *Mater. Horiz.* **2015**, *2*, 37−53.
(38) Ogieglo, W.; Wormeester, H.; Wessling, M.; Benes, N. E. Spectroscopic Ellipsometry Analysis of a Thin Film Composite Membrane Consisting of Polysulfone on a Porous α-Alumina Support. *ACS Appl. Mater. Interfaces* **2012**, *4*, 935−943.
(39) Li, D.; Carette, M.; Granier, A.; Landesman, J. P.; Goullet, A. In Situ Spectroscopic Ellipsometry Study of TiO_2 Films Deposited by Plasma Enhanced Chemical Vapour Deposition. *Appl. Surf. Sci.* **2013**, *283*, 234−239.
(40) Ogieglo, W.; Wormeester, H.; Wessling, M.; Benes, N. E. Temperature-Induced Transition of the Diffusion Mechanism of n-Hexane in Ultra-Thin Polystyrene Films, Resolved by In-Situ Spectroscopic Ellipsometry. *Polymer* **2013**, *54*, 341−348.
(41) Hor, J. L.; Wang, H.; Fakhraai, Z.; Lee, D. Effect of Physical Nanoconfinement on the Viscosity of Unentangled Polymers during Capillary Rise Infiltration. *Macromolecules* **2018**, *51*, 5069−5078.

https://doi.org/10.1021/acsami.3c07254
ACS Appl. Mater. Interfaces 2023, 15, 40913−40922

(42) Sibeko, M. A.; Saladino, M. L.; Luyt, A. S.; Caponetti, E. Morphology and Properties of Poly(methyl methacrylate) (PMMA) Filled with Mesoporous Silica (MCM-41) Prepared by Melt Compounding. *J. Mater. Sci.* **2016**, *51*, 3957−3970.
(43) Holland, B. J.; Hay, J. N. The Effect of Polymerisation Conditions on the Kinetics and Mechanisms of Thermal Degradation of PMMA. *Polym. Degrad. Stab.* **2002**, *77*, 435−439.
(44) Hor, J. L.; Wang, H.; Fakhraai, Z.; Lee, D. Effects of Polymer−Nanoparticle Interactions on the Viscosity of Unentangled Polymers under Extreme Nanoconfinement during Capillary Rise Infiltration. *Soft Matter* **2018**, *14*, 2438−2446.
(45) Venkatesh, R. B.; Lee, D. Conflicting Effects of Extreme Nanoconfinement on the Translational and Segmental Motion of Entangled Polymers. *Macromolecules* **2022**, *55*, 4492−4501.
(46) de Jongh, P. E.; Eggenhuisen, T. M. Melt Infiltration: an Emerging Technique for the Preparation of Novel Functional Nanostructured Materials. *Adv. Mater.* **2013**, *25*, 6672−6690.
(47) Chen, M.; Wu, L.; Zhou, S.; You, B. A Method for the Fabrication of Monodisperse Hollow Silica Spheres. *Adv. Mater.* **2006**, *18*, 801−806.

https://doi.org/10.1021/acsami.3c07254
ACS Appl. Mater. Interfaces 2023, 15, 40913−40922